U. of Iowa 90-13

NEW VOYAGER
RADIO SPECTROGRAMS OF URANUS

by

W. Calvert[1] and D. Tsintikidis

June 1990

Department of Physics and Astronomy
The University of Iowa
Iowa City, IA 52242

[1]Currently at Tokyo Denki University, Ishizaka,
Hatoyama, Hiki, Saitama, 350-03 JAPAN

Abstract. New, high-resolution spectrograms of the Voyager-2 radio observations at Uranus have been produced from the original, six-second Planetary Radio Astronomy (PRA) data and these show a number of new features which were not obvious in previous versions. Among these new features are the detailed structure of the so-called "broadband-bursty" (b-bursty) emissions, unexpected sloping striations in the "smooth high-frequency" (SHF) component, and the overlap of these two components during the first rotation after closest approach. In addition, we have found a slightly different planetary rotation rate from the b-bursty emissions, and at the initial onset of the SHF component, what appears to be the shadow of a uranian plasmasphere. These new spectrograms were prepared using a special "dithering" algorithm to show signal strengths as gray shadings, and the data were also manually cleaned to suppress noise and interference. This produced spectrograms of exceptional quality and certain details of their production on a stand-alone personal computer are also discussed.

INTRODUCTION

Cyclotron Emissions. The two Voyager spacecraft, now both beyond Neptune and heading away from the Solar System, have provided unique observations of intense, non-thermal radio emissions from all four of the giant planets [Warwick, et al., 1979a, 1979b, 1981, 1982, 1986, 1990]. Comparable also to the AKR emissions from the Earth [Gurnett, 1974], the strongest such radio emissions have been found to consist of extraordinary-mode radiation at the electron cyclotron frequency from the planets' magnetic polar regions, although other, weaker emissions have also been reported [see Desch, et al., 1987; Evans, et al., 1987; Leblanc, et al., 1987]. Since these cyclotron emissions are beamed in directions which are presumably fixed with respect to the planetary magnetic field, they have proven quite useful for measuring the planetary rotation rates [Desch, et al., 1986]. Moreover, they are also of considerable intrinsic interest, since such planetary cyclotron radio emissions now seem to be a ubiquitous feature of all planetary magnetospheres.

PRA Spectrograms. The main instruments for detecting these planetary radio emissions with Voyager are the Planetary Radio Astronomy (PRA) experiments of Warwick, et al. [1977]. Identical on both of the Voyagers and consisting of swept-frequency radio receivers for frequencies up to about 40 MHz, the PRA instruments are capable of detecting both the wave signal strength and certain aspects of the wave

polarization at 198 frequencies every six seconds (in its most commonly-used mode). It thus produces millions of measurements during each of the planetary encounters, for periods lasting from more than two months at Jupiter to only a week or two at Uranus and Neptune. These data are generally displayed as "radio spectrograms" or "dynamic spectra" showing the received signal strength as a gray or colored shading as a function of the frequency and time. Figure 1, for example, is a radio spectrogram of Voyager-2 PRA observations at Uranus, in this case for the 53 lowest frequency channels extending up to about 1 MHz. Such radio spectrograms, which show simultaneously the occurrence, frequency, and behavior of the radio emissions, have proven quite useful in studies of these emissions.

Preview. The purpose of this paper is to present new, high-resolution spectrograms of the PRA radio observations at Uranus and to point out certain features which they show somewhat better than previous versions. It is divided into two parts, the first presenting examples of the new spectrograms and describing the new features we have found and the second discussing certain aspects of producing these spectrograms. This will be followed by a discussion of certain points and a summary of our conclusions. Finally, we will include as appendices certain details of our implementation for others who may wish to adopt similar techniques.

Scope. Our search for new features has not been exhaustive, nor do we consider any of our interpretations conclusive. Instead, the spirit of this paper is to show the

excellent spectrograms we have been able to produce and to highlight a number of interesting topics for possible future study.

NEW SPECTROGRAMS

The Uranus Encounter. Among all of the planets visited by the Voyagers, Uranus is unique because of its highly-inclined rotation axis and its tilted, offset magnetic field, and this has caused its cyclotron emissions to come only from the previously-hidden night side of the planet. As a consequence, they were not detected until just before closest approach when the night hemisphere first came into view. The period of principal interest therefore extended this time until these signals were lost for the purpose of making spectrograms about eight days later. (Although later signals have been reported by Desch, et al. [1986], they occurred outside the data set we had available and they were also probably too weak to make good spectrograms, judging from the amplitude decreases during the eight days we have examined.) During this period Voyager passed in front of and close to the planet and then away from it in its night hemisphere, almost in the ecliptic plane at an angle of about 35° to its south polar rotation axis [Stone, 1987]. Combined with the tilted magnetic field, this produced significant excursions in the magnetic latitude and longitude of Voyager during each planetary rotation after encounter, as illustrated by Figure 1 of Farrell and Calvert [1989a]. As a consequence,

there were repeated encounters with the beamed emissions of the planet as Voyager receded, as discussed by Leblanc, et al. [1987].

Principal Components. The two principal cyclotron emission components, which appear alternately in Figure 1, are designated the "broadband bursty" or "b-bursty" and the "smooth high frequency" or "SHF". Both of these are attributed to hollow emission cones from the magnetic south polar region of the planet [see Kaiser, et al., 1987; Zarka and Lecacheux, 1987; Farrell and Calvert, 1989a,b; and references therein]. The former occupies a broad, thin cone with a half-angle of roughly 85°, whereas the latter occupies a smaller, almost-filled cone with a half-angle of roughly 60°. The b-bursty emissions appeared first, at about 15:30 SCET (spacecraft event time, equivalent to UT at the Earth) on 24 January 1986, and the first SHF appeared about one to three hours later, depending on the frequency, at 16:30 to 18:30 SCET. Thereafter, the signals of these two emissions appeared alternately and gradually became weaker as Voyager moved further from the planet. During most of this period after closest approach, Voyager was well inside the broad conical beam of the b-bursty emissions, effectively exploring that pattern from the inside out and back again during each revolution, whereas for about half of the time it was also inside the SHF beam, sometimes passing almost directly through its axis [see Kaiser, et al., 1987]. The b-bursty emissions in Figure 1 are characterized by rapid changes in sometimes less than a minute, whereas the SHF emissions are characterized by smooth variations often lasting for hours and conspicuous "biteouts" at the higher frequencies as Voyager crossed its emission-cone axis [*ibid.*].

First B-Bursty. The first the b-bursty emissions observed with Voyager are shown in greater detail in Figure 2. The principal feature of this emission appears to be a rising component having a relatively sharp and seemingly enhanced low-frequency edge. The rising component, sloping upward from about 600 kHz at 15:27 SCET to 750 kHz at 15:40 SCET, is attributed to the b-bursty emission cone having somewhat smaller emission cone angle at the higher frequencies, although the difference is not very great, amounting to only about 2° for this event, from roughly 85° to 87°. The lower edge of this pattern, on the other hand, sloping downward from about 650 kHz at 15:24 SCET to 300 kHz at 15:35 SCET, appears to be a cutoff imposed by propagation, since there seems to be an enhancement at this edge, presumably caused by the caustic focus of wave ray paths like that which causes the so-called "skip-zone focusing" of shortwave radio propagation [see Davies, 1965]. This feature thus suggests reflection by some sort of plasma obstacle between the source and Voyager, possibly a uranian plasmasphere.

Multiple B-bursts. Figure 3 shows this same b-bursty emission on a smaller scale along with the other SHF and b-bursty emissions which followed. Note in this case, and also in Figure 4, that the b-bursty signals appear to occur with a regular spacing of about one hour and twenty minutes (e.g. between the first burst at 15:30 and those at 16:50, 18:10, 19:55, and 20:40 SCET; as well as also between the pair of bursts at 16:10 and 17:25). Although this could be a temporal pulsation of the source, it is more likely that this corresponds to a multiple-lobe emission pattern for the b-bursty source, whereupon the observed spacing would imply an azimuthal angle of about 50° between

the lobes, since Voyager was then moving approximately parallel to the b-bursty emission cone edge at rate of about 38° per hour (see Farrell and Calvert [1989a], Fig. 5(a)).

Overlap of the B-Bursty and SHF. Note also in Figures 3 and 4 that these bursts extend well into the region occupied by the SHF emissions, implying that the overall emission cones of these two components overlap. In other words, there were still significant b-bursty emissions well inside the cone at angles also occupied by the SHF emissions. However, these emissions were significantly weaker than those at the cone edge, by as much at 20 dB at 500 kHz, according to Figure 5, and this accounts for their difficulty of detection later when Voyager was considerably further from the planet. Their apparent absence on previous spectrograms, on the other hand, is attributed to the logarithmic averaging that was used, as will be discussed below.

Maximum Frequency. It is also striking in Figure 3 how steady the upper frequency limit of the SHF emissions remains after about 18:30 SCET. This suggests that this frequency, of about 900 kHz, is an absolute upper limit for the SHF emissions, and hence also the maximum frequency emitted by Uranus, since none of the other emissions (see Figure 1) extend quite as high. If this is interpreted according to the rule-of-thumb that cyclotron emission requires a plasma frequency of less than about one-third of the cyclotron frequency [Benson and Calvert, 1979], this implies a plasma frequency of about 300 kHz, and hence a source plasma density at the highest frequencies of the order of 10^3 electrons per cubic centimeter.

Apparent Plasmaspheric Shadow. Notice also that there was a clearcut onset of the SHF emissions at progressively higher frequencies in Figure 3, extending from about 200 kHz at 16:30 SCET to about 900 kHz at 18:30 SCET. This can be interpreted as the geometric shadow of an obstacle between the source and Voyager, and since the source altitude at the cyclotron frequency presumably decreases with the frequency, its variation with frequency suggests that Voyager was viewing over that obstacle so as to see progressively lower altitudes in the source at later times, as Voyager moved toward higher southern magnetic latitudes. This same effect was also found to occur for the AKR at the Earth, where it was attributed to occultation by the Earth's plasmasphere [Gurnett, 1974]. The subsequent SHF onsets and terminations, on the other hand, as shown in Figure 1 and below in Figure 5, for example, seem to lack this feature and show a much more ragged and variable pattern. In other words, the SHF emissions observed later did not seem to show the same kind of smooth edge, and that is attributed to the different observation geometry at those times, since only during closest approach was Voyager close enough to the planet and at sufficiently low magnetic latitudes for the wave path from the SHF source to have intercepted a possible plasmasphere. The b-bursty emissions which occurred earlier, however, appear to have missed this shadow and exhibited a different one of their own, and this tends to confirm that the b-bursty and SHF emissions must originate from different locations on the planet, as previously reported by Farrell and Calvert [1989b] and others, since otherwise these two emissions would presumably have shown the same shadow.

SHF Striations. Figure 5 shows the SHF emissions during the next full rotation after closest approach. Notice in this figure the curious asymmetric striations on the SHF component, extending gradually upward from about 300 kHz at 12:30 SCET on January 25 to about 450 kHz at 16:00 SCET. These striations also possibly extend across the SHF signal gap [see Kaiser, et al., 1987] to as far as 700 kHz at 20:00 SCET, although it is hard to be certain that those striations are the same feature. (The other horizontal striations in this figure, however, could be artifacts of our cleaning process, as discussed below.) Although only a weak modulation amounting to one or two decibels, these striations appear to be a consistent feature of the SHF emissions, since they also seem to occur during other rotations. They are obviously not faraday rotation, since they lack its characteristic reciprocal-frequency-squared spacing, and no suitable interpretation of this feature has yet been found. Because of its asymmetry across the signal gap, it does not appear to be a function of the emission cone angle, but instead is probably a function of the observing longitude, since that was changing progressively during these periods.

Periodic "Arcs". Also shown very faintly on the lefthand side of Figure 5, in between the b-bursty and SHF emissions at about 700 kHz and 12:30 SCET, are the so-called "periodic arcs" of Warwick, et al., [1986] and Kistler, [1988]. Figure 6 is an enlargement of this feature, also modified to increase the contrast for weak signals (the regular white gaps being signal outages while the instrument was operating in a different mode). Although the arc shape of these features is not obvious here, this figure shows

about ten occurrences, and for the seven most prominent ones not obscured by a data outage, the repetition period was found to be 9.7 ± 0.1 minutes.

B-Bursty Structure. Figures 7, 8, and 9 show enlarged examples of the b-bursty emissions after the second, fourth, and sixth rotations of the planet after closest approach. As predicted by Farrell and Calvert [1989a], a gap in these emissions occurred near the center of the pattern in Figure 7, between about 2:05 and 2:30 SCET. This is attributed to Voyager passing outside the b-bursty emission cone momentarily and then back in again. On either side of this gap there was a more-or-less symmetrical envelope for the emissions, although the detail within this envelope did not seem to show such symmetry. Instead, it appeared to show a roughly periodic meandering between high and low frequencies (e.g. in Figure 7 starting at 1:00, 3:00, and 3:45 SCET and in Figure 8 starting at 17:50), but with phases which were not symmetrical across the gap. In addition, these features seem to sometimes disappear completely, as they did just after where the gap was expected at about 20:00 SCET in Figure 8 and for the whole period before the expected gap position at 23:45 SCET on 28 January in Figure 9. These periodic meanderings of the b-bursty emissions thus seem to be neither stable from one event to the next nor are they a simple function of the beam angle, since that would have produced symmetry across the gap. This fine structure, on the other hand, because of its wide frequency range, its regular spacing, and its tendency to form loops, is believed to be the most-likely uranian counterpart of the well-known jovian decametric arcs of Warwick, et al. [1979a].

Last B-Bursty. Figure 10 show a final occurrence of what are believed to be b-bursty emissions another four rotations after Figure 9. These emissions appear at the far right in Figure 1 and they are in fact the last uranian radio signals clearly detectable on the PRA spectrograms (excluding the later signals reported by Desch, et al. [1986]). These signals are presumably those after the gap in the b-bursty pattern and it is not known why they suddenly reappeared for only one rotation. Only a hint to the same kind of internal structure appears, more comparable to that in Figure 9 than the earlier figures presumably because these signals were so weak they tended to merge with the receiver noise.

Dayside O-Mode. As a final example of the PRA spectrograms, a special one of the dayside ordinary emission of Desch, et al. [1987] is shown in Figure 11, with the contrast adjusted for weak signals. Although it could be an artifact of our cleaning process, similar weak signals are found to occur extending from about 450 kHz up to about 600 kHz. Since the intervening frequency channels between this feature and 250 kHz upper limit of the main emissions are particularly noisy, the gap between this and the signals at lower frequencies could be instrumental and the actual upper frequency limit for these emissions might be as high as 600 kHz.

SPECTROGRAM TECHNIQUES

History. The technique of displaying radio data using gray scales began with the so-called "ionograms" produced by the swept-frequency, pulsed radio transmitters (similarly called "ionosondes") which have been used to detect radio echoes from the Earth's ionosphere since the 1940's [see Davies, 1965]. In this case the ionospheric echoes were displayed as light-intensity modulations on an oscilloscope and then photographed with a moving-film camera. The oscilloscope was adjusted to produce a single thin line perpendicular to the direction of film motion, and when this line was photographed as the film moved, a continuous picture of the ionospheric echoes was produced showing the echo delay (of up to a few tens of milliseconds) on the one axis versus the frequency (generally 0.5 to 30 MHz) on the other. For swept-frequency radio receivers, both in satellites and on the ground, similar techniques were applied to display the frequency versus time, for example, to record the spectrum of magnetospherically-propagated lightning whistlers at VLF frequencies [see Helliwell, 1965]. Eventually such ionograms and spectrograms became standard tools of geophysical and astronomical radio research.

Digital Techniques. With the advent of computers, of course, such data were digitized and the moving-film cameras were replaced by digital plotters and printers. With this came the problem of representing the gray or colored scales on devices which

were not really designed for that purpose and of handling relatively large quantities of digital data. Originally requiring large central computing facilities with expensive digital plotters, it has now become feasible to accomplish this same task with the new generation of high-performance personal computers, as we have done to produce the spectrograms in this paper. Although not without some difficulties (primarily of having to develop one's own software and of having to cope with certain instrumental limitations), we have found this not only quite feasible but also quite convenient, since different techniques could be experimented with and the results seen almost immediately. During this effort, special attention was focused upon (1) the techniques for producing gray scales, (2) the interpolation and averaging which are needed to fit the available data to spectrograms of a given size, and (3) the problem of dealing with instrumental interference and noise, as will now be discussed.

Gray Scale. As can be seen upon careful examination of the spectrograms above, their gray shadings actually consist of a varying patterns of dots somewhat like those in the well-known halftone process used for printing photographs. Such dot patterns are generally produced by one of two techniques. The first is to divide the image into rectangular pixels of so-many-dots by so-many-dots and then assign specific dot patterns within each pixel according to level of shading which is required. The second is to calculate each of the dots separately according to some sort of computer algorithm. The latter is called 'dithering', presumably because it produces what appears to be a fine-scale agitation of the image. Random dithering, for example, can be produced quite

simply by plotting the individual dots according to whether or not the input signal value exceeds the result of a random-number calculation. Although requiring extensive calculations for each dot, this produces a random dot pattern having an average dot density which is statistically proportional to the original signal. In producing our spectrograms we have used dithering, but instead of this random dithering, we have used a different algorithm which is not only faster but better for this purpose.

Dithering Algorithm. The dithering algorithm which we have used is a variation of the so-called "Floyd-Steinberg" algorithm [see Ulichney, 1987, Ch. 8]. This quite clever and efficient algorithm, which was adapted for us with the help of L. J. Granroth of the University of Iowa, is described in Appendix A. In this algorithm the dots are plotted one line at a time in sequentially opposite directions (in our case vertically, going up and down from left to right) and track is kept of whether the dots which have already been plotted are ahead or behind at representing the appropriate average density. The resulting density error is then distributed in certain proportions to the signals that remain to be plotted in both the current and next adjacent lines. This produces a compact, regular pattern of dots which is locally smooth and hence less distracting than random dithering.

Interpolation and Averaging. Our next problem was that the data and plotting intervals generally do not match. In Figure 1, for example, there are only about fifty measurements vertically, corresponding to the individual PRA frequency channels, whereas there are 115,200 six-second measurements to be plotted horizontally during

the eight days of this spectrogram. Since the dot image we were capable of printing consists of about 800 dots vertically by 1920 dots horizontally, this means we must interpolate vertically and average horizontally in order to fit the available data into a single spectrogram. This means sharing one measurement among 16 dots in the vertical direction while at the same time combining 60 of those interpolated measurements to produce a single dot in the horizontal direction. The former was handled by straightforward linear interpolation (actually log interpolation in signal strength since it is the logarithmic values which are plotted). The latter, however, poses a more difficult question, since the choice of averaging technique can significantly affect which signals are emphasized in the final spectrogram. For instance, if one averages the logarithmic signal values, as has been done extensively in the past, one is actually plotting the geometric mean of the data to be averaged, and this will emphasize weak, steady signals over impulsive strong ones. For the PRA data from Uranus this is particularly significant, since that data includes both the relatively-smooth SHF component and the intermittent, but sometimes much stronger (by as much as 30 dB or more) b-bursty emissions, and as a result, the b-bursty emissions were often suppressed in previous versions of the spectrograms. In producing our spectrograms we have gone to the opposite extreme by plotting the maximum signals during each of the averaging periods, this being both quick for the computer and serving to emphasize the b-bursty component. Moreover, we did not distinguish the two polarization channels of the instrument [see

Leblanc, et al., 1987]. but simply let the stronger of the two dominate in making these spectrograms.

Interference. Although the best radio data available for the outer planets, the PRA data are beset by high noise levels and severe interference from other instruments on the spacecraft. One of its channels near 900 kHz, for example, was always fully saturated, corresponding to a steady interference which was more than fifty decibels stronger than the receiver threshold. Most other channels also suffered from relatively high noise levels as well as variable interference which came and went, and sometimes changed frequency as the different instruments on board turned on and off or changed their operating modes. It was therefore necessary to deal with a rat's nest of different interfering signals in order to produce quality spectrograms, and earlier on we tried a number of different automatic algorithms for this purpose. All of these, however, failed rather badly, sometimes eliminating the signals we wanted to keep and sometimes introducing new ones which should not have been there. As a result, we switched to manual cleaning using an interactive program designed for that purpose.

Cleaning Procedure. Our interactive cleaning program used a screen display like Figure 4 in which the spectrogram and the values versus time were plotted for a given PRA channel (Figure 4 actually being a screen dump of this program's display). Upon command, the program would generate a moveable box in the lower panel to select the data to be modified, and then upon further command, the selected data could be translated to a different reference level, substituted for with the log average of the two

adjacent frequency channels, or else restored to their original values. We quickly developed sufficient skill with this program to recognize the interference and either simply move it out of the way by translating it to the receiver's background noise level or, at some sacrifice of spectral resolution, substitute the adjacent-channel average. Most of the interference was quite obvious and characterized by square onsets and pulse trains that were synchronized with the Voyager instrument clock. At other times, however, the interference was not so obvious and it was sometimes quite hard to distinguish it from the actual signals, particularly in the midst of the highly-variable b-bursty component.

Translation Algorithm. In our cleaning of the data it was realized that simple translation of the data would not be adequate, since the data values are represented logarithmically, because whatever real signals might have been present along with the noise would have been changed too significantly. We therefore devised a compromise translation algorithm in which data near a selectable amplitude reference level were translated directly to a new target reference level, whereas those which were significantly stronger (e.g. by 5 dB or so) were left near their original levels by displacing them inversely proportional to the log signal difference above the reference level. In this fashion, even for large changes in the reference level, strong signals remained strong and very strong signals were practically unaffected.

DISCUSSION

Black-and-White versus Color. Although color spectrograms are used quite frequently nowadays for more dramatic impact or sometimes to highlight certain features, the black-and-white spectrograms we have presented here offer certain other advantages. First of all, they are cheaper to produce and reproduce and they yield publications which can be readily photocopied. However, they also yield the more subtle advantage of sometimes showing better certain features with varying amplitude like the SHF striations in Figure 5. The perception of contrast between the blues, yellows, and reds of a color spectrogram, it seems, is frequently too strong to show well a feature which crosses these color boundaries. For this same reason, on the other hand, this makes it harder to produce good black-and-white spectrograms, since relatively small amplitude errors in the background noise level show up so well, as they do in our Figures 6 and 11. Nonetheless, we feel there is good reason for black-and-white spectrograms, even if all of us were wealthy enough to afford color.

Gray Backgrounds. In our spectrograms we have adjusted the gray-scale range (represented by the third and fourth numbers of the code at the upper right of each spectrogram, in 0.2 dB steps) to produce a light gray background. This was done intentionally, based on prior experience with the satellite topside-sounder ionograms [see Franklin, et al., 1969], in order to maximize the detection of weak signals, and we

recommend this practice even though it does sometimes show our lack of complete cleaning.

Cleaning Errors. One should be aware that our manual cleaning of the data could both introduce artificial features or eliminate others which were incorrectly identified as noise. It also tends to introduce horizontal striations like those in Figures 5, 6, and 11, and this should be allowed for in studying our spectrograms. Nonetheless, we have done our best to remove the interference without sacrificing the integrity of the data, and if this becomes an issue, the reader is advised to produce his own spectrograms from the original PRA data.

48-Second Data. One should be aware that the 48-second PRA data sets widely distributed by M. L. Kaiser of GSFC are logarithmic averages of the data (i.e. geometric means) rather than actual arithmetic averages. As discussed previously, this will tend to favor weak steady signals over impulsive strong ones, and for Uranus it thus tends to suppress the b-bursty component. This is best illustrated by a specific example, to wit: If one log-averages four signals, three at a level 20 dB and the fourth at a level of 60 dB, the result is 30 dB, and this corresponds to a signal which is only ten times stronger than the weaker, steady signals. However, the actual arithmetic average is at a decibel level of 53.98, which is about 2,500 times stronger than the weaker signals. The error is therefore a factor of 250, and this is the sort of error which can be expected when the b-bursty signals in the lower panel of Figure 5 are log-averaged with the receiver

noise. One must thus be quite careful in assessing the strength of such bursty signals when log-averaging is used.

Dithering. The use of systematic dithering, as we have done here, can sometimes introduce patterns of its own, especially when the display resolution is relatively coarse, as it is in Figure 4. Although this pattern is relatively easy to ignore, like a wallpaper or clothing pattern usually is, one should keep it in mind when searching for patterns in the data. On the other hand, random dithering is often much worse, since it tends to produce random groupings and trends which attract the eye and are quite hard to ignore. It was primarily for this reason that we discarded the random dithering that we had used originally in favor of the Floyd-Steinberg algorithm.

Apparent Plasmasphere. In order to confirm our interpretation of the apparent plasmaspheric shadow in Figure 3, we have performed the following calculation: For various time and frequencies along this SHF onset we determined the position of Voyager in magnetic coordinates (again with the help of L. J. Granroth) and calculated the spherical angle between that position and the SHF source of Farrell and Calvert [1989b]. Using this angle, we then plotted the path of Voyager with respect to the source, as shown in Figure 12, and drew ray paths from the source to Voyager, starting at the appropriate source altitude for cyclotron emission, assuming a $1/r^3$ magnetic field-strength variation. This diagram is thus a composite of Voyager's position with respect to the source in the planes also containing the magnetic center of the planet, and the ray paths therefore only roughly represent their actual three-dimensional trajectories.

However, this yielded a set of ray paths which were quite suggestive of a plasmaspheric shadow, for a plasmasphere extending out to about three uranian radii. The density of this plasmasphere is hard to estimate from these ray path because of their glancing angles at reflection, but it probably corresponds to a plasma frequency which was not much less than about one-quarter of the wave frequency, since that would support reflection at angles of up to about 15° to the plasmapause surface (assuming plane stratification and neglecting the magnetic field at reflection). The plasmapause density might thus be comparable to that at the earth, or about 150 electrons per cubic centimeter.

Alternatives and Future Work. Although Figure 12 is quite suggestive of a uranian plasmasphere, none is predicted for Uranus by Selesnick and Richardson [1986], nor are there other observations to confirm its existence, since Voyager did not come close enough for direct plasma measurements. It is therefore important to pursue this further and to consider other possible interpretations of the smooth SHF onset. Such further work might include (1) three-dimensional ray tracing using a more specific plasmapause model, (2) an analysis of the wave polarization at the onset to search for the mode-splitting which can accompany a remote plasma reflection when the emitted polarization is not perfectly circular, and (3) a consistent analysis of the B-bursty shadow using the same plasmaspheric model. Possible alternative interpretations might include the shadow being some sort of limit cone for emission, such as that possibly caused by wave refraction at the source (i.e., perpendicular to the source refractive index gradient, which

for extraordinary-mode waves at low plasma densities in a polar source is approximately perpendicular to the magnetic field and hence not inconsistent with Figure 12). Such matters, however, are beyond the scope of this paper and are left for future study.

Planetary Rotation Period. A shift of 139.2 ± 0.5 hours is required to align the b-bursty signals in Figure 7 with those in Figure 10, observed eight revolutions later, the uncertainty being estimated from visual alignment of the two b-bursty events. This of course implies a planetary rotation period of 17.40 ± 0.06 hours. We thus find a rotation period which is about one percent longer than that quoted by Desch, et al. [1986], of 17.24 ± 0.01 hours, and the difference is more than twice our estimated alignment uncertainty.

Possible Errors. The principal sources of error in this measurement are our identification of the event in figure 10 as a b-bursty event comparable to that in Figure 7, and of course, our the assumption that these two events occur for the same rotation phase. As already discussed by Desch, et al. [1986], the instrumental timing errors, the motion of Voyager during the period, and the light-speed delay from Uranus to Voyager do not contribute significantly. Since we do not yet understand why the b-bursty comes and goes, nor what determines its exact direction of emission, further study of this emission component is required to fully justify this measurement. On the other hand, the method of Desch, et al. [1986] also suffers from this same limitation, along with the added uncertainty of not being quite sure which of the uranian emission components is dominating the measurement. This, in fact, might significantly affect their measurement,

since their technique depended upon detecting the average signal above the receiver threshold and that could change as the signals become weaker with distance, from initially being dominated by the SHF component to later becoming dominated by the stronger yet intermittent b-bursty component. What is more, if this were the case, it could introduce up to one-half rotation error over the 42 rotations they used, and this would account for a one percent discrepancy.

SUMMARY

In this paper we have presented high-resolution spectrograms of the Voyager PRA observations at Uranus and pointed out a number of features which were not obvious in previous versions. These features include the detailed pattern of the b-bursty emissions showing arc-like structures which are not replicated from one revolution to the next, abrupt onsets of both the first b-bursty and the SHF emissions near closest approach which could indicate shadowing of the source by a possible uranian plasmasphere, overlap of the b-bursty and SHF emission patterns, and unexpected sloping striations on the SHF emissions. We have also presented further observations of the previously-reported periodic arcs and the dayside ordinary-mode emissions and found a new final occurrence of the b-bursty emissions which seems to indicated about one percent error in the previously-measured planetary rotation rate. We have also discussed

various aspects of producing spectrograms on personal computers and introduced the important improvement of using the Floyd-Steinberg dithering algorithm.

Acknowledgements. We are grateful to L. J. Granroth for suggesting the use of dithering to make spectrograms and for introducing to us the Floyd-Steinberg algorithm, as well as for his extensive help throughout the entire project. We also thank W. M. Farrell for numerous useful discussions; and D. R. Evans and J. W. Warwick, of Radiophysics, Inc., for providing the six-second Voyager data. This work was supported by NASA Grant NAGW-1206 as a part of the Uranus Data Analysis Program (UDAP).

REFERENCES

Benson, R. F., and Calvert, W., ISIS 1 observations at the source of auroral kilometric radiation, *Geophys. Res. Let.*, 6, 479-482, 1979.

Calvert, W., The source location of certain jovian decametric radio emissions, *J. Geophys. Res., 88,* 6165-6170, 1983.

Davies, K., *Ionospheric Radio Propagation,* National Bureau of Standards Monograph 80, U. S. Government Printing Office, 1965.

Desch, M. D., J. E. P. Connerney and M. L. Kaiser, The rotation period of Uranus, *Nature, 322*, 42-43, 1986.

Desch, M. D., and M. L. Kaiser, Ordinary mode radio emission from Uranus, *J. Geophys. Res., 92*, 15,211-15,216, 1987.

Evans, D. R., J. H. Romig and J. W. Warwick, Bursty radio emissions from Uranus, *J. Geophys. Res., 92*, 15,206-15,210, 1987.

Farrell, W. M., and W. Calvert, The source location and beaming of broadband bursty radio emissions from Uranus, *J. Geophys. Res., 94*, 217-225, 1989.

Farrell, W. M., and W. Calvert, Source location of the Smooth High-Frequency Radio Emissions from Uranus, *Geophys. Res. Lett., 16*, 341-344, 1989.

Franklin, C. A., R. J. Bibby, and N. S. Hitchcock, Data acquisition and processing system for mass producing topside ionograms, *Proc. IEEE, Special Issue on Topside Sounding*, June 1969.

Gurnett, D. A., The Earth as a radio source: Terrestrial kilometric radiation, *J. Geophys. Res., 79*, 4227, 1974.

Helliwell, R. A., *Whistlers and Related Ionospheric Phenomena,* Stanford University Press (Stanford, California), 1965.

Kaiser, M. L., M. D. Desch, and S. A. Curtis, The sources of Uranus' dominant nightside radio emissions, *J. Geophys. Res., 92,* 15,169-15,176, 1987.

Kistler, A. C., Voyager 2 Detection of uranian hectometric radio arcs (Master's Thesis), University of Iowa, Iowa City, Iowa, 1988.

Leblanc, Y., M. G. Aubier, A. Ortega-Molina, and A. Lecacheux, Overview of the Uranian radio emissions: Polarization and constraints on source locations, *J. Geophys. Res., 92,* 15,125-15,138, 1987.

Ness, N. F., M. H. Acuña, A. W. Behannon, L. F. Burlaga, J. E. P. Connerney, R. P. Lepping, and F. M. Neubauer, Magnetic fields at Uranus, *Science, 233,* 85-89, 1986.

Selesnick, R. S., and J. D. Richardson, Plasmasphere formation in arbitrarily oriented magnetospheres, *Geophys. Res. Lett., 13,* 624-627, 1986.

Stone, E. C., The Voyager 2 encounter with Uranus, *J. Geophys. Res., 92,* 14,873-14,876, 1987.

Ulichney, R., *Digital Halftoning,* The MIT Press (Cambridge, Mass.), 1987.

Warwick, J. W., J. B. Pearce, R. G. Peltzer, and A. C. Riddle, Planetary radio astronomy experiment for Voyager missions, *Space Sci. Rev., 21,* 309-327, 1977.

Warwick, J. W., J. B. Pearce, A. C. Riddle, J. K. Alexander, M. D. Desch, M. L. Kaiser, J. R. Thieman, T. D. Carr, S. Gulkis, A. Boischot, C. C. Harvey, and B. M. Pedersen, Voyager 1 Planetary radio astronomy observations near Jupiter, *Science, 204,* 995-998, 1979a.

Warwick, J. W., J. B. Pearce, A. C. Riddle, J. K. Alexander, M. D. Desch, M. L. Kaiser, J. R. Thieman, T. D. Carr, S. Gulkis, A. Boischot, Y. Leblanc, B. M. Pedersen, and D. H. Staelin, Planetary radio astronomy observations from Voyager 2 near Jupiter, *Science, 206,* 991-995, 1979b.

Warwick, J. W., J. B. Pearce, D. R. Evans, T. D. Carr, J. J. Schauble, J. K. Alexander, M. L. Kaiser, M. D. Desch, M. Pedersen, A. Lecacheux, G. Daigne, A. Boischot, and

C. H. Barrow, Planetary radio astronomy observations from Voyager 1 near Saturn, *Science, 212,* 239-243, 1981.

Warwick, J. W., D. R. Evans, J. H. Romig, J. K. Alexander, M. D. Desch, M. L. Kaiser, M. Aubier, Y. Leblanc, A. Lecacheux, and B. M. Pedersen, Planetary radio astronomy observations from Voyager 2 near Saturn, *Science, 215,* 582-587, 1982.

Warwick, J. W., D. R. Evans, J. H. Romig, C. B. Sawyer, M. D. Desch, M. L. Kaiser, J. K. Alexander, T. D. Carr, D. H. Staelin, S. Gulkis, R. L. Poynter, M. Aubier, A. Boischot, Y. Leblanc, A. Lecacheux, B. M. Pedersen, and P. Zarka, Voyager 2 radio observations of Uranus, *Science, 233,* 102-106, 1986.

Warwick, J. W., D. R. Evans, G. R. Peltzer, R. G. Peltzer, J. H. Romig, C. B. Sawyer, A. C. Riddle, A. E. Schweitzer, M. D. Desch, M. L. Kaiser, W. M. Farrell, T. D. Carr, I. De Pater, D. H. Staelin, S. Gulkis, R. L. Poynter, A. Boischot, F. Genova, Y. Leblanc, A. Lecacheux, A. Lecacheux, B. M. Pedersen, and P. Zarka, Voyager planetary radio astronomy at Neptune, *Science, 246,* 1498-1501, 1990.

Zarka, P., and A. Lecacheux, Beaming of Uranian nightside kilometric radio emissions and inferred source location, *J. Geophys. Res., 92,* 15,177-15,187, 1987.

Appendix A: The Floyd-Steinberg Dithering Algorithm

The gist of our implementation of the Floyd-Steinberg dithering algorithm [Ulichney, 1987], expressed in Turbo Pascal, is as follows:

```
if Signal [CurrentY] > MidSignal then
   begin
     Putpixel... {the Turbo Pascal Routine for making dots};
     Error := Signal [CurrentY] - BlackSignal;
   end
 else
   begin
     {No dot is plotted when the Signal is less than MidSignal}
     Error := Signal [CurrentY] - WhiteSignal;
   end;


Signal [NextY]     := Signal [NextY]     + (7 * Error) div 16;
ErrArr [PreviousY] := ErrArr [PreviousY] + (3 * Error) div 16;
ErrArr [CurrentY]  := ErrArr [CurrentY]  + (5 * Error) div 16;
ErrArr [NextY]     := ErrArr [NextY]     +      Error  div 16;
```

In this algorithm, the curly brackets enclose comments and the square brackets designate array indices, all of these indices being vertical dot positions, with CurrentY, PreviousY,

and NextY referring to the y coordinate (vertical) of the current, previous, and next dots to be plotted. The constants BlackSignal, WhiteSignal, and MidSignal are the signal values which should appear as solid black, solid white, and halfway in between. Putpixel is the software routine which makes a dot.

After this routine is executed for each of the dots in a vertical line, the resulting error array (designated "ErrArr" and set to zero before each line) is added to the next array of signal values to be plotted. The first program statement (which here occupies the first ten lines) plots a dot if the signal exceeds midrange and calculates the error that this causes with respect to the desired black and white levels. This error is then divided into sixteen parts (sixteen because that's easy in a binary computer) and distributed to the next point of the same line and in differing proportions to the adjacent points of the next line.

Appendix B. Implementation

Equipment. An IBM-compatible machine was chosen because of its low cost, its widespread availability and upgradability, and its wealth of available software. The equipment we used, all "clones" built by other manufacturers and assembled ourselves, began with a simple XT (Intel 8086) computer, a Hercules monochrome display, a Hewlett-Packard InkJet printer, and a 30-megabyte hard disk, although this was eventually upgraded to an 80386 processor, an EGA display, an H-P DeskJet printer,

and a 630-megabyte hard disk. However, even for this advanced configuration, the cost was considerably less than our annual computing budget had been for previous years, and we thus recommend not skimping on equipment now that such power is available at such reasonable cost. On the other hand, where budgets are limited, there is no reason that a simple setup like our original XT configuration could not have been used quite productively, since the principal difference was simply a matter of speed and the difficulty of having to reload large data sets from floppy disks.

Software. The programming language we used was Turbo Pascal, and, although any such language would be suitable, this is recommended over Fortran or BASIC, even for the beginner, because it fosters a better programming style and is so convenient to use. Using a single, relatively small hard disk initially, we reformatted the data into compact files containing only the data we needed. At the same time, we applied an instrument calibration using calibration tables supplied by M. L. Kaiser of GSFC, although we kept the results in eight-bit form to save space. These data were written into a different file for each of the 48-minute spacecraft clock cycles, these files being of fixed length with sufficient space for each of the 480 measurement periods in a clock cycle and labeled with the spacecraft clock value. In this fashion, we avoided the difficult problem of having to sort the data into chronological order. The data set for Uranus thus occupied about six megabytes, whereas in its original form it required roughly fifty megabytes and had to be loaded piecemeal into our original, small-disk configuration.

FIGURE CAPTIONS

Fig. 1. A spectrogram of the radio emissions observed with Voyager 2 at Uranus. In this and subsequent figures the frequency is vertical, the time horizontal, and stronger signals are shown as darker shadings. The coded numbers at the upper right are the number of 48-minute data periods included (here 240), the number of six-second periods to the start of plotting (176), the black and white data levels in 0.2 Db steps (27 and 80), and the starting spacecraft clock value (26825).

Fig. 2. The first b-bursty emissions observed with Voyager, showing their trend toward higher frequencies and an apparent caustic focus cutoff on the lower left.

Fig. 3. A spectrogram showing (1) the overlap of the b-bursty and SHF emissions near closest approach (see also Figure 4), (2) a sudden, systematic onset of the SHF emissions which is attributed to shadowing by a uranian plasmasphere, and (3) a steady upper cutoff for the latter, presumably corresponding to the maximum possible frequency of cyclotron emission.

Fig. 4. A low-resolution spectrogram comparable to that in Figure 3, along with the accompanying calibrated signals values for 500 kHz. Note how much stronger the b-bursty signals often are and how far they extend into the following SHF emissions.

Fig. 5. SHF emissions showing its dropout above about 450 kHz at 16:00-18:00 SCET and unexplained sloping striations extending from lower left to upper right.

Fig. 6. The previously-identified periodic arcs, at about 700 kHz in the middle of this spectrogram, with fainter ones extending further toward the left. Below are the b-bursty emissions on the left and the SHF on the right, both overexposed to emphasize the arcs.

Fig. 7. Detail of the b-bursty emissions, showing the gap of Farrell and Calvert [1989a] at about 2:15 SCET.

Fig. 8. B-bursty emissions showing different detail two revolutions later (the feature at 16:30 SCET being a type-III solar radio burst).

Fig. 9. B-bursty emissions an additional two planetary rotations after Figure 8.

Fig. 10. The final b-bursty emissions seen with Voyager 2, an additional four revolutions after Figure 9.

Fig. 11. The dayside O-mode emissions of Desch and Kaiser [1987], at 125-250 kHz and possibly also above about 450 kHz, between 4:00 and 8:00 SCET.

Fig. 12. The positions of Voyager with respect to the SHF source and the magnetic center of Uranus, projected into a common plane with the source in one direction, for the times and frequencies of the SHF onset in Figure 3, showing as the envelope of straight-line ray paths the apparent shadow of a uranian plasmasphere.

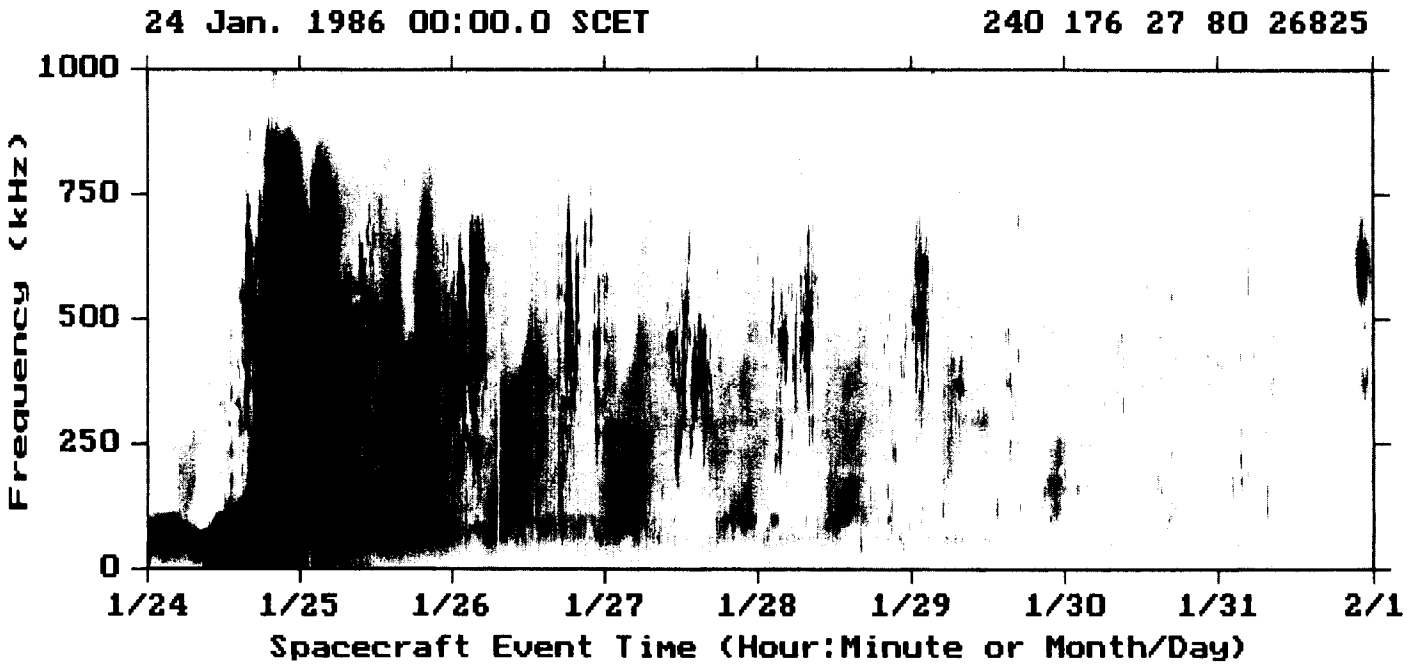
24 Jan. 1986 00:00.0 SCET
240 176 27 80 26825
1000
750
500
250
0
Frequency (kHz)
1/24
1/25
1/26
1/27
1/28
1/29
1/30
1/31
2/1
Spacecraft Event Time (Hour:Minute or Month/Day)

Figure 1

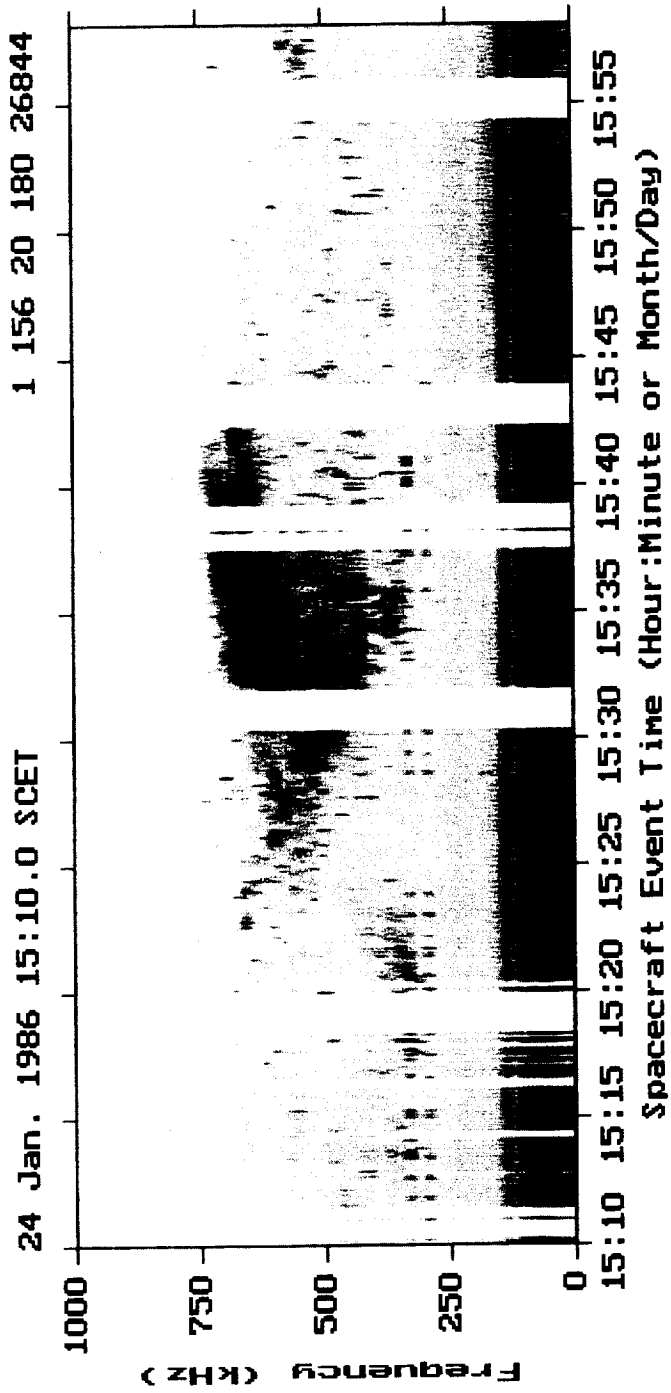
24 Jan. 1986 15:10.0 SCET
1 156 20 180 26844
1000
750
500
250
0
Frequency (kHz)
15:10 15:15 15:20 15:25 15:30 15:35 15:40 15:45 15:50 15:55
Spacecraft Event Time (Hour:Minute or Month/Day)

Figure 2

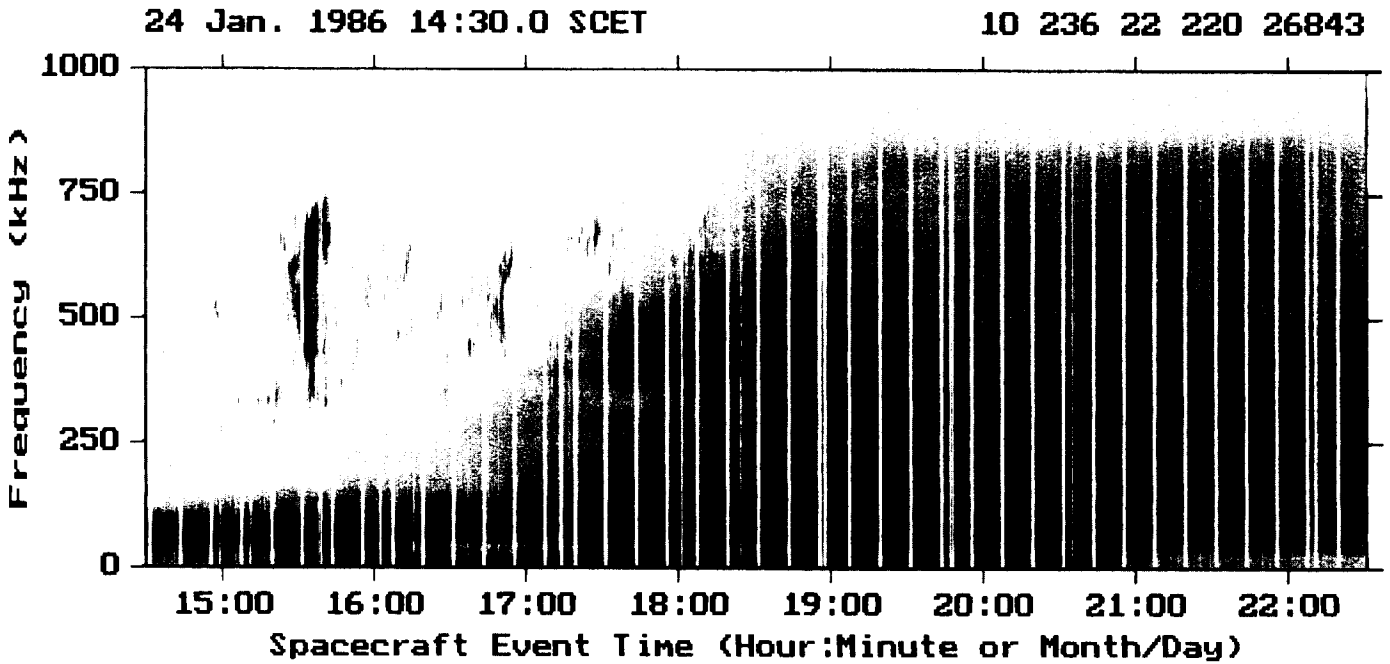
24 Jan. 1986 14:30.0 SCET
10 236 22 220 26843
1000
750
500
250
0
Frequency (kHz)
15:00
16:00
17:00
18:00
19:00
20:00
21:00
22:00
Spacecraft Event Time (Hour:Minute or Month/Day)

Figure 3

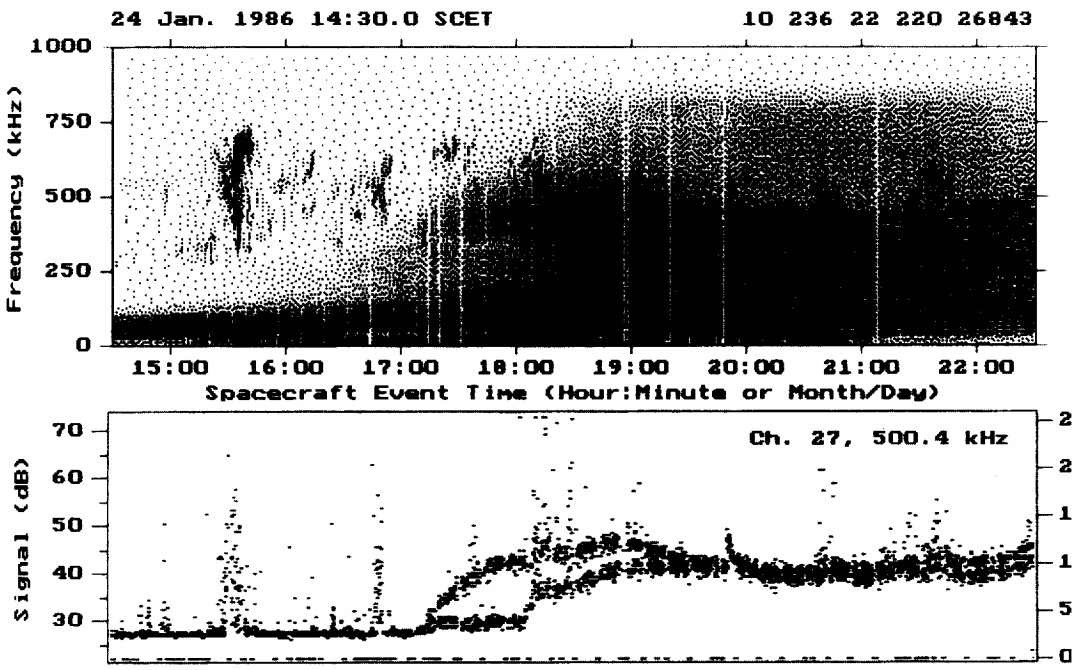
24 Jan. 1986 14:30.0 SCET
10 236 22 220 26843
Frequency (kHz)
1000
750
500
250
0
15:00
16:00
17:00
18:00
19:00
20:00
21:00
22:00
Spacecraft Event Time (Hour:Minute or Month/Day)
Signal (dB)
70
60
50
40
30
Ch. 27, 500.4 kHz
2
2
1
1
5
0

Figure 4

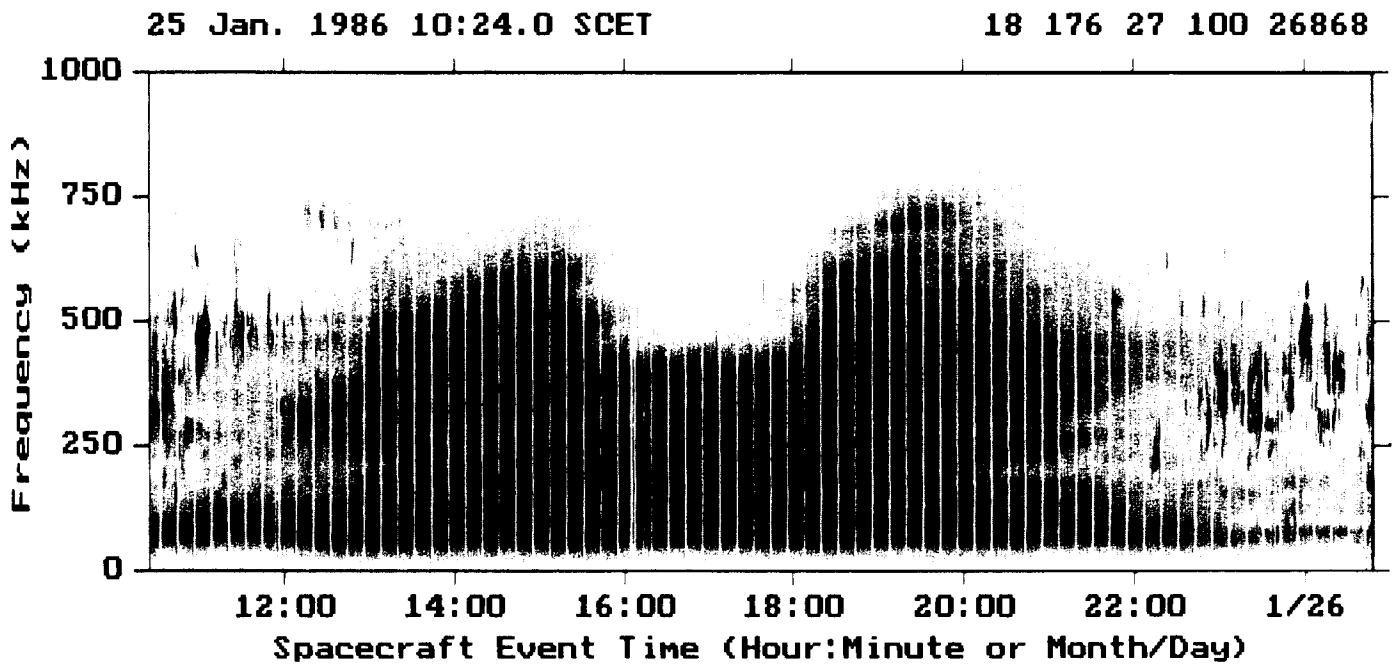
25 Jan. 1986 10:24.0 SCET
18 176 27 100 26868
1000
750
500
250
0
Frequency (kHz)
12:00
14:00
16:00
18:00
20:00
22:00
1/26
Spacecraft Event Time (Hour:Minute or Month/Day)

Figure 5

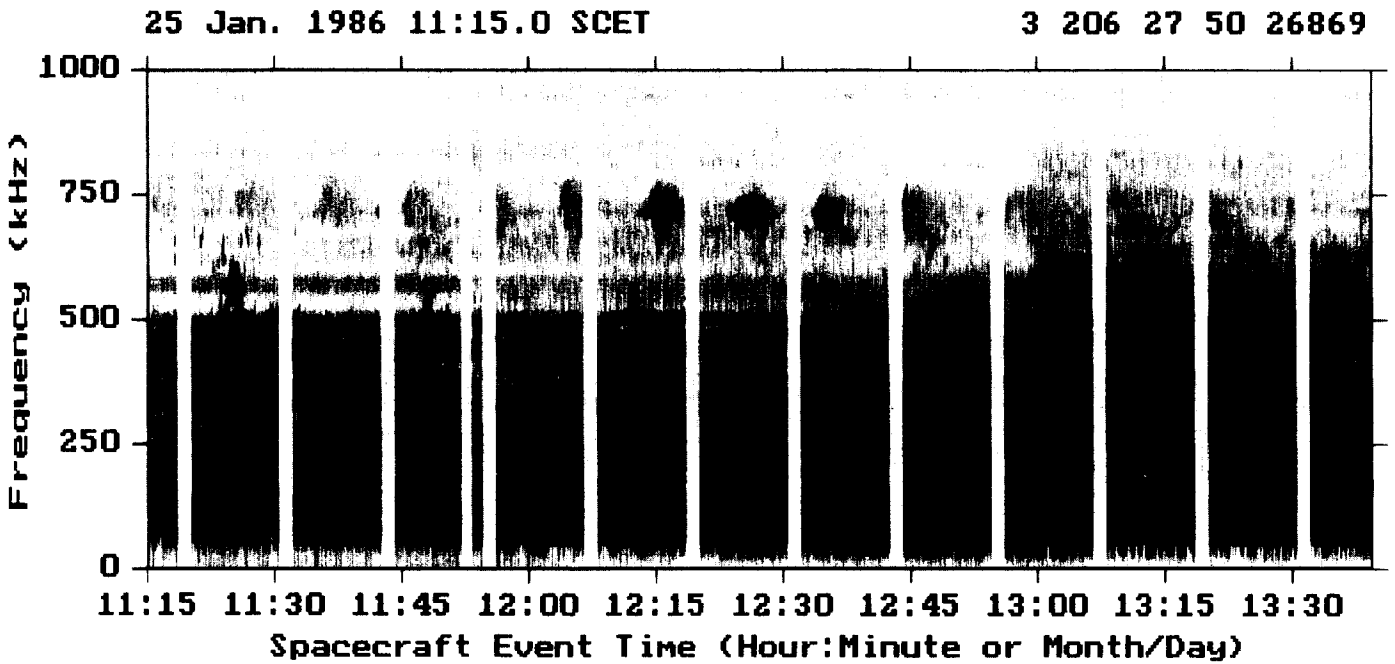
25 Jan. 1986 11:15.0 SCET
3 206 27 50 26869
1000
750
500
250
0
Frequency (kHz)
11:15
11:30
11:45
12:00
12:15
12:30
12:45
13:00
13:15
13:30
Spacecraft Event Time (Hour:Minute or Month/Day)

Figure 6

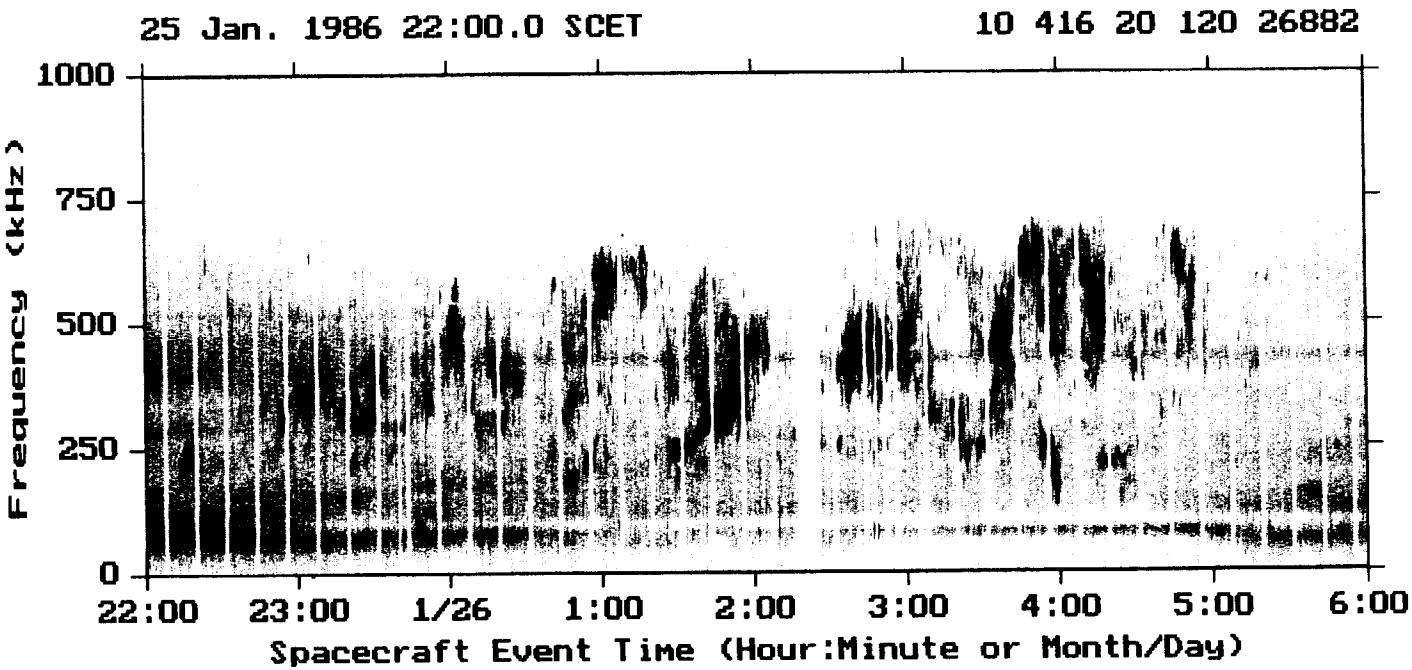
25 Jan. 1986 22:00.0 SCET
10 416 20 120 26882
1000
750
500
250
0
Frequency (kHz)
22:00
23:00
1/26
1:00
2:00
3:00
4:00
5:00
6:00
Spacecraft Event Time (Hour:Minute or Month/Day)

Figure 7

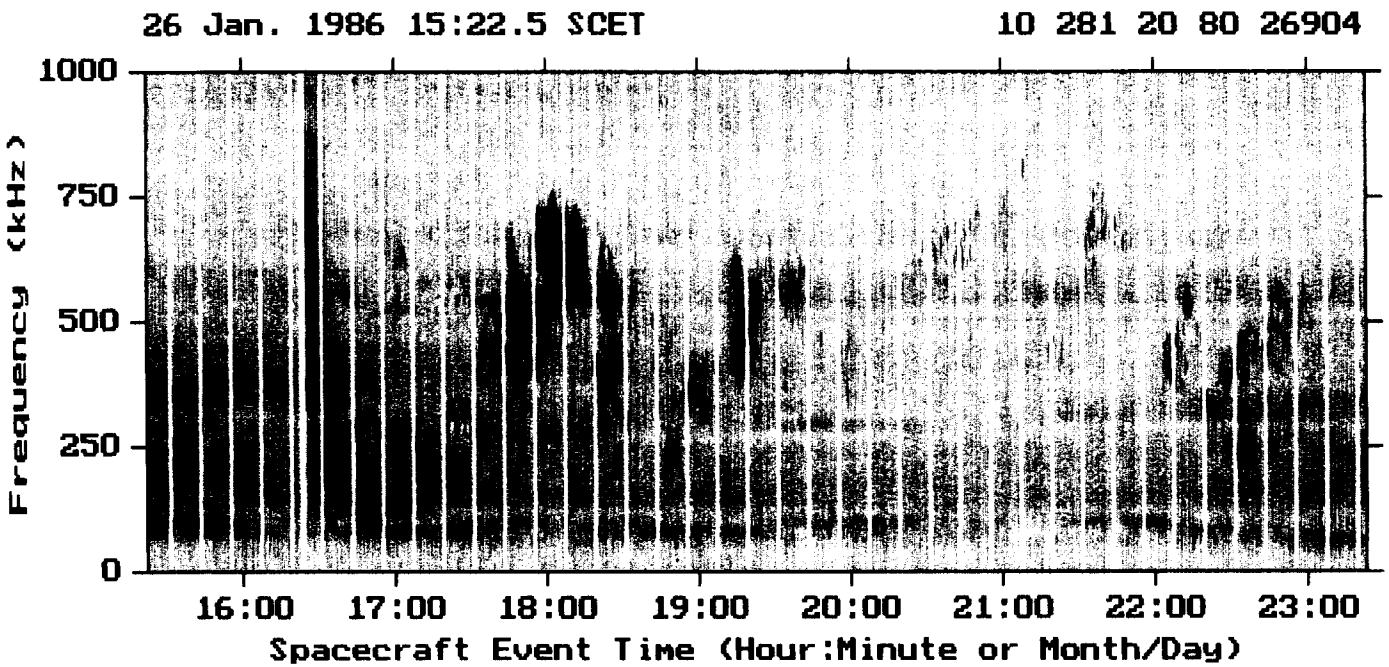
26 Jan. 1986 15:22.5 SCET
10 281 20 80 26904
1000
750
500
250
0
Frequency (kHz)
16:00
17:00
18:00
19:00
20:00
21:00
22:00
23:00
Spacecraft Event Time (Hour:Minute or Month/Day)

Figure 8

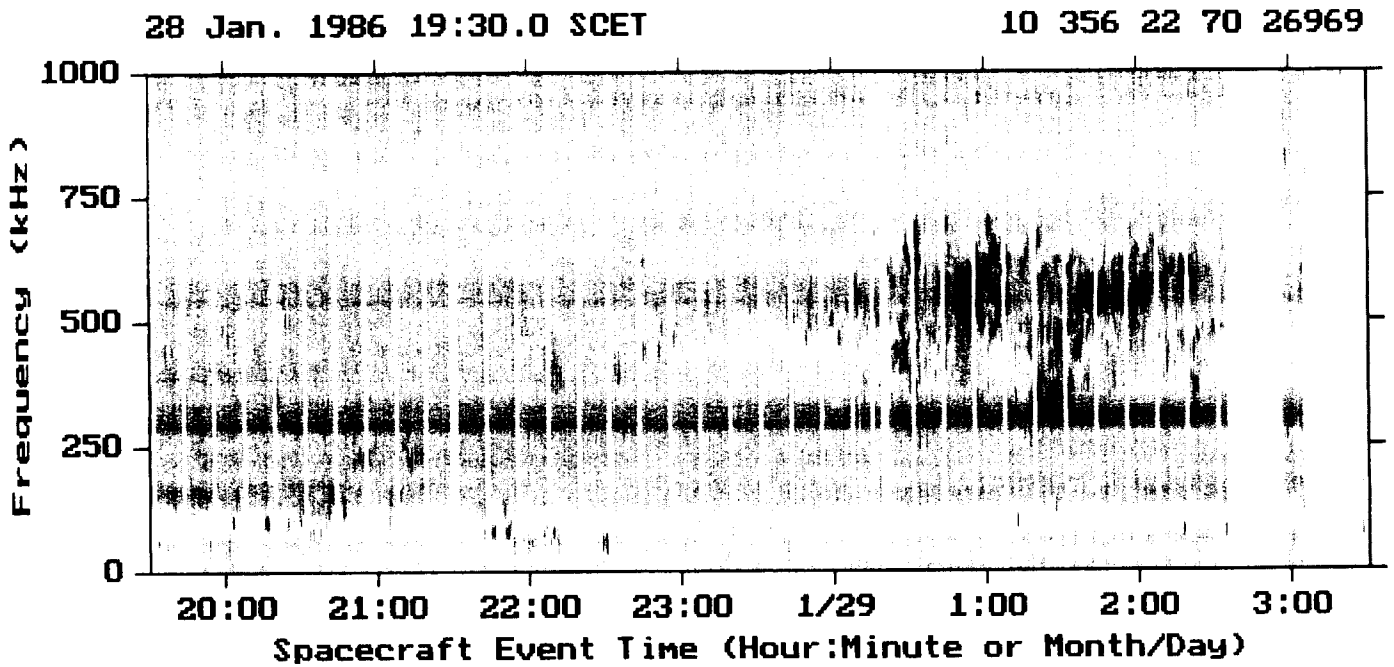
28 Jan. 1986 19:30.0 SCET
10 356 22 70 26969
1000
750
500
250
0
Frequency (kHz)
20:00
21:00
22:00
23:00
1/29
1:00
2:00
3:00
Spacecraft Event Time (Hour:Minute or Month/Day)

Figure 9

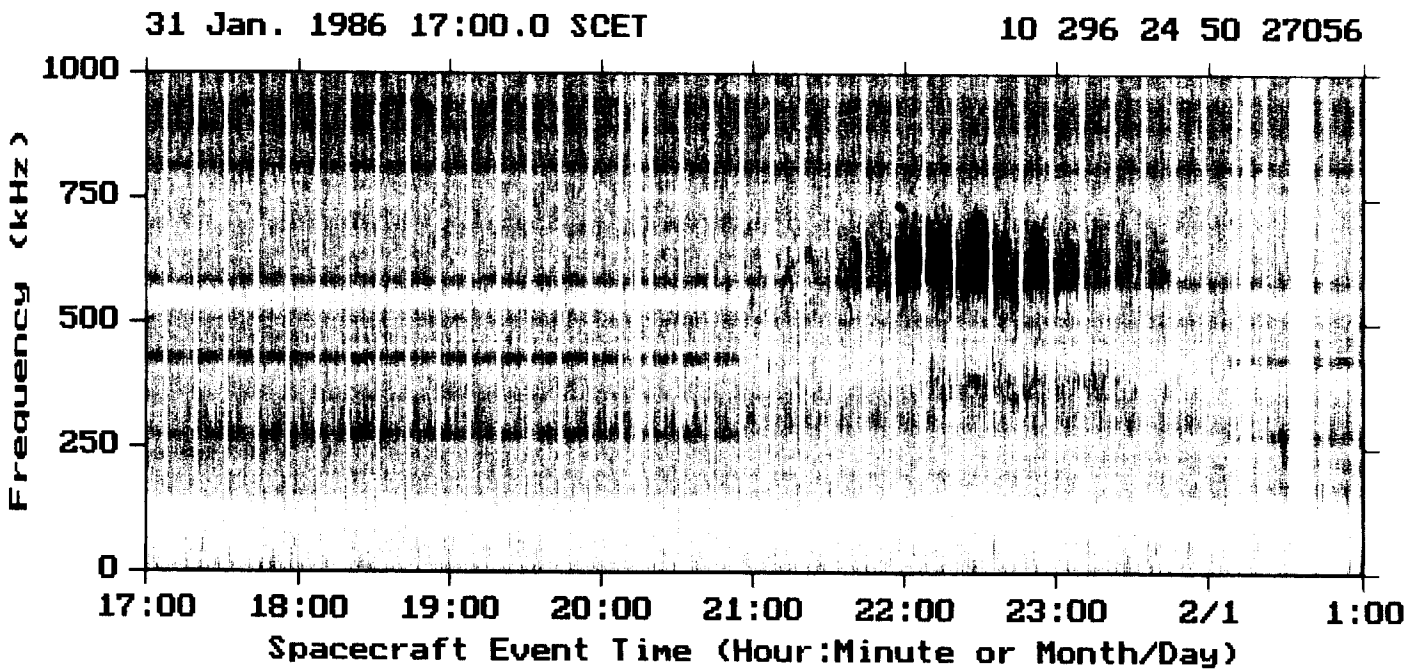
31 Jan. 1986 17:00.0 SCET
10 296 24 50 27056
1000
750
500
250
0
Frequency (kHz)
17:00
18:00
19:00
20:00
21:00
22:00
23:00
2/1
1:00
Spacecraft Event Time (Hour:Minute or Month/Day)

Figure 10

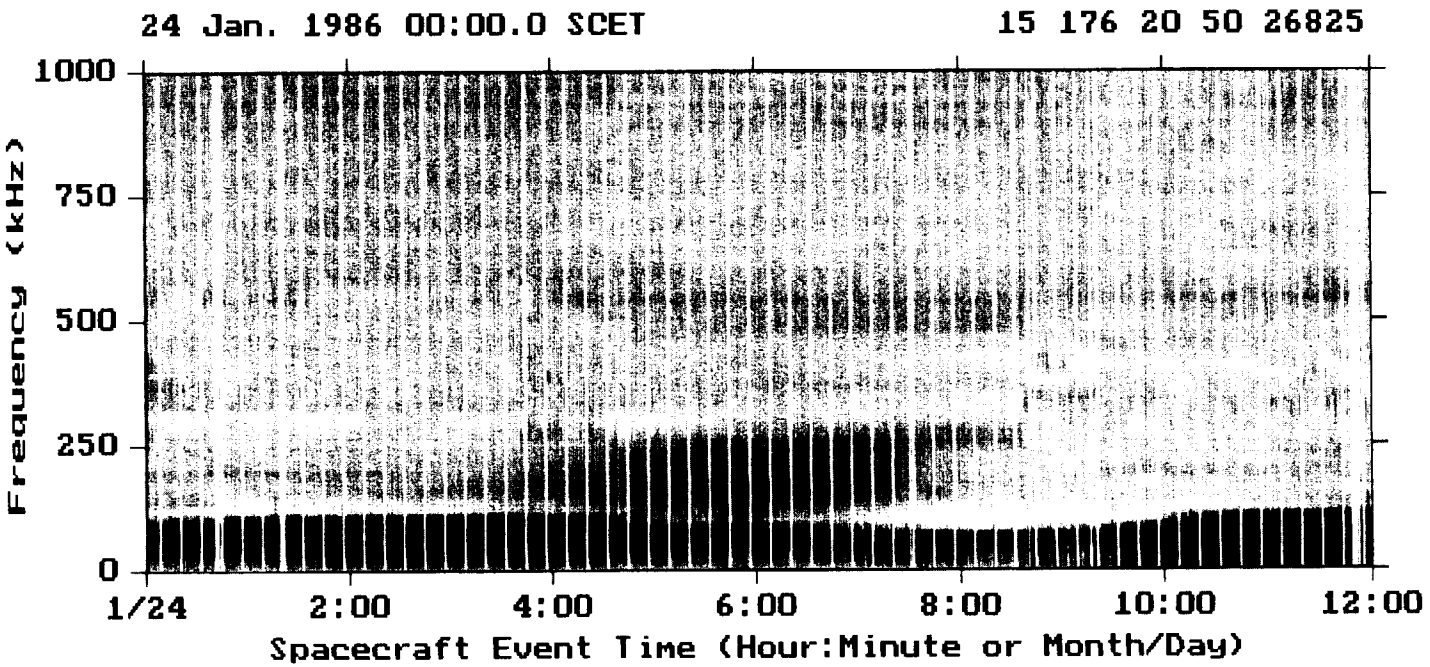
24 Jan. 1986 00:00.0 SCET
15 176 20 50 26825
1000
750
500
250
0
Frequency (kHz)
1/24
2:00
4:00
6:00
8:00
10:00
12:00
Spacecraft Event Time (Hour:Minute or Month/Day)

Figure 11

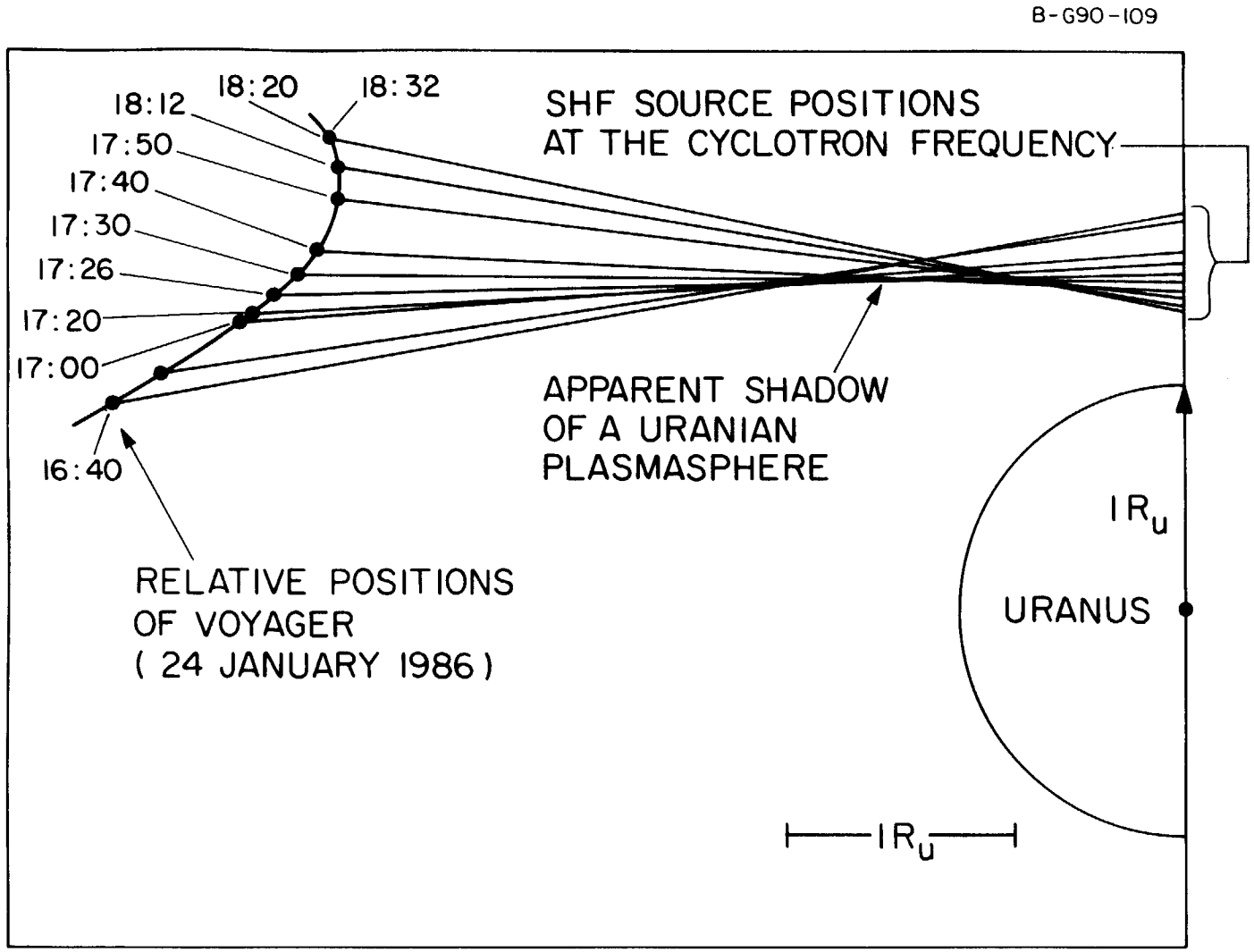
B-G90-109
18:12
18:20
18:32
17:50
17:40
17:30
17:26
17:20
17:00
16:40
SHF SOURCE POSITIONS
AT THE CYCLOTRON FREQUENCY
APPARENT SHADOW
OF A URANIAN
PLASMASPHERE
RELATIVE POSITIONS
OF VOYAGER
(24 JANUARY 1986)
1 R_u
URANUS
1 R_u

Figure 12